RSC Advances

ROYAL SOCIETY OF CHEMISTRY

www.rsc.org/advances

Graphical Abstract

(*This manuscript is submitted to RSC Advances as a full paper*)

Facile hydrothermal synthesis and electrochemical properties of orthorhombic $LiMnO_2$ cathode materials for rechargeable lithium batteries

Shulin Chen[1], Feifei Cao[2], Fan Liu[1], Quanjun Xiang[1], Xionghan Feng[1], Lihu Liu[1], Guohong Qiu*[,1]

[1] College of Resources and Environment, Huazhong Agricultural University, Wuhan, 430070, P. R. China

[2] College of Sciences, Huazhong Agricultural University, Wuhan, 430070, P. R. China

* Corresponding authors: G.H. Qiu, qiugh@mail.hzau.edu.cn, Tel/Fax: +86(0)27 87280271

TOC Text

Pure-phased and aluminum-doped orthorhombic $LiMnO_2$ (*o*-$LiMnO_2$) cathode materials with high discharge capacity and cyclic stability are prepared by a simple one-step hydrothermal treatment of $MnCl_2$, EDTA, LiOH, $AlCl_3$ and NaClO solutions. Mixing $LiMn_2O_4$ and doping aluminum improve the electrochemical lithium storage performance of *o*-$LiMnO_2$.

TOC Graphic

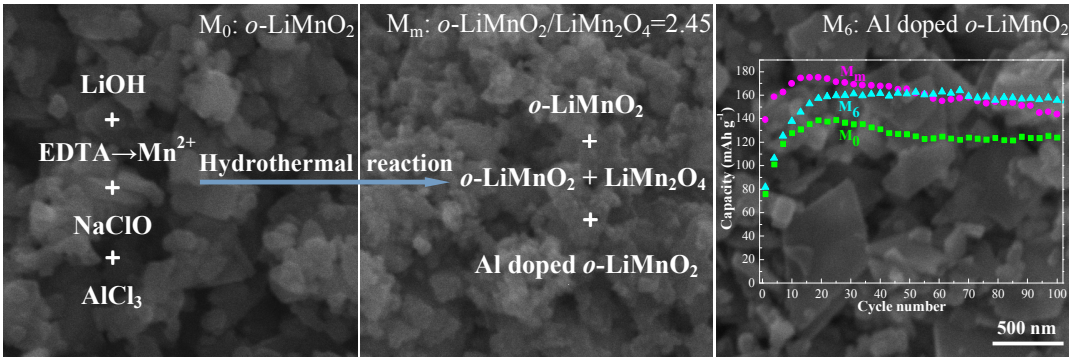

Facile hydrothermal synthesis and electrochemical properties of orthorhombic $LiMnO_2$ cathode materials for rechargeable lithium batteries

Shulin Chen[1], Feifei Cao[2], Fan Liu[1], Quanjun Xiang[1], Xionghan Feng[1], Lihu Liu[1], Guohong Qiu*[,1]

[1] College of Resources and Environment, Huazhong Agricultural University, Wuhan, 430070, P. R. China

[2] College of Sciences, Huazhong Agricultural University, Wuhan, 430070, P. R. China

* Corresponding author: G.H. Qiu, qiugh@mail.hzau.edu.cn, Tel/Fax: +86(0)27 87280271

Abstract: Pure-phased, $LiMn_2O_4$-mixed and aluminum-doped orthorhombic $LiMnO_2$ (*o*-$LiMnO_2$) cathode materials with high discharge capacity and excellent cyclic stability were prepared by one-step hydrothermal reaction of $MnCl_2$, EDTA, LiOH, $AlCl_3$ and NaClO solutions. Chemical composition and aluminum content were affected by temperature and the concentration of LiOH, NaClO and $AlCl_3$. A mixed phase of Mn_3O_4 and *o*-$LiMnO_2$, pure-phased *o*-$LiMnO_2$, and a mixed phase of *o*-$LiMnO_2$ and $LiMn_2O_4$ were formed with increasing the concentration of NaClO from 0.08 to 0.25 mol L^{-1} at 180 ^oC for 24 h. Adding EDTA and NaClO facilitated the formation of *o*-$LiMnO_2$. Al/Mn molar percent ratios in doped *o*-$LiMnO_2$ were 0.34, 0.58, 0.91, and 1.22 when Al/Mn molar ratios in hydrothermal system were controlled as 0.05, 0.10, 0.15, and 0.20, respectively. Mixing $LiMn_2O_4$ and doping Al improved the discharge capacity and cyclic stability of *o*-$LiMnO_2$. *o*-$LiMnO_2$, the mixture with *o*-$LiMnO_2$/$LiMn_2O_4$ mass ratio of 2.45, and doped *o*-$LiMnO_2$ with Al/Mn molar percent ratio of 0.58 exhibited the initial discharge capacity of 76, 139, and 82 mAh g^{-1}, and cycling capacity of 124, 144, and 156 mAh g^{-1} after 100 cycles, respectively. This work facilitates the preparation and electrochemical performance improvement of *o*-$LiMnO_2$.

Keywords: Orthorhombic $LiMnO_2$; Cathode materials; Lithium battery; Hydrothermal synthesis; Electrochemical properties

1. Introduction

Lithium ion batteries have been widely investigated for high-power applications including electric vehicles, plug-in hybrid electric vehicles, and hybrid electric vehicles [1,2]. As for the first commercially successful cathode materials of lithium batteries, $LiCoO_2$ needs to be substituted due to its high cost, toxicity, and low discharge capacity about 140-150 mAh g^{-1} [3-5]. Alternatively, *o*-$LiMnO_2$ and spinel $LiMn_2O_4$ composites have been considered as the promising cathode materials for rechargeable lithium ion batteries owing to their abundant resources, low cost, environmental friendship, safety, high voltage, and good rate capability, which has been a hot research topic in the field of chemical power source [6,7]. However, $LiMn_2O_4$ exhibits lower discharge capacity of 110-120 mAh g^{-1} and cyclic stability due to accelerated Mn dissolution at an elevated temperature cycling and structural instability for Jahn-Teller distortion [4,5,7-9]. *o*-$LiMnO_2$ shows a higher theoretical discharge capacity of 285 mAh g^{-1}, which is almost twice that of spinel $LiMn_2O_4$ [10]. Additionally, *o*-$LiMnO_2$ shows a lower capacity fade rate, which is commonly affected by chemical structures and composition. Therefore, much effort has been devoted to the fabrication of pure-phased and doped *o*-$LiMnO_2$ particles for cathode materials of lithium batteries [4,10-12].

At present, *o*-$LiMnO_2$ samples are usually prepared by high temperature solid-state reactions [4,11], sol-gel process [13], ion exchange [7], and hydrothermal method [3,10,14]. As for the above methods, micro-structured precursors including Mn_2O_3, $MnCO_3$, $NaMnO_2$, and γ-MnOOH should be first fabricated for the consequent transformation of *o*-$LiMnO_2$. Multi-step and high temperature reactions will increase the energy consumption and cost. Recently, *o*-$LiMnO_2$ nano-particles were prepared under mild hydrothermal conditions from $KMnO_4$, $MnCl_2$, and LiOH sources, but too much lithium source, Li/Mn molar ratio more than 30, was used [15]. One-step hydrothermal method was used to prepare uniform nano-sized $LiMnO_2$ with low energy consumption, and the morphologies could be easily controlled, and the as-obtained $LiMnO_2$ showed excellent electrochemical performance [3,16]. Generally, for the hydrothermal synthesis of *o*-$LiMnO_2$, a high concentration of LiOH was required, and Li/Mn molar ratio in raw materials was usually larger than

13 [15-17]. In order to reduce cost for industrial application, the preparation of *o*-$LiMnO_2$ using low Li/Mn molar ratio is highly desirable.

The weak cyclic stability of *o*-$LiMnO_2$ is associated with Jahn-Teller distortion for the change of manganese oxidation states during charge/discharge process, and the partial substitution of Mn by metal ions is commonly used to stabilize the layered structure [11,12,18]. Cr^{3+} and Al^{3+} ions prevent manganese ion migration during cycling, reducing the tendency of the layered structure converting to the more stable spinel [11]. Cr substitution decreases the capacity fade rate of *o*-$LiMnO_2$, and the reversible capacity maintains 160 mAh g^{-1} after 50 cycles with C/5 rate [18]. Co doped $LiMnO_2$ was formed using ion exchange of $NaMnO_2$ synthesized by a solid state reaction, and kept 200 mAh g^{-1} even after 20 cycles at 0.1 mA cm^{-2} over the potential range of 2.6-4.85 V [7]. Ni doped $LiMnO_2$ also showed 198 mAh g^{-1} with retention ratio of 96% after 25 cycles at C/3, and the layered structures exhibited no phase change during the charge/discharge process [19]. The indium- and sulfur-doped $LiMnO_2$ samples with orthorhombic structure as cathode materials of lithium batteries showed excellent electrochemical capacity of 267.9 mAh g^{-1} [20]. In other words, doping would remarkably improve $LiMnO_2$ electrochemical performance including specific capacity and cyclic stability. Hydrothermal synthesis of doped $LiMnO_2$ was usually conducted using the as-prepared precursors, such as $MnCO_3$ [11,18] and Mn_2O_3 [18-20]. To the authors' knowledge, there was no facile one-step hydrothermal process to prepare metal doped *o*-$LiMnO_2$.

As for hydrothermal synthesis, pure-phased $LiMnO_2$ was difficult to synthesize likely due to the further oxidation of $LiMnO_2$ to form Li_2MnO_3 [21]. An appropriate redox rate should be controlled to obtain single-phased $LiMnO_2$ with low-valent manganese. Under refluxing conditions, sodium hypochlorite (NaClO) could oxidize Mn(II) source to form uniform ramsdellite-type manganese oxide with various morphologies [22]. $MnPO_4 \cdot H_2O$ and hureaulite containing low-valent Mn(III/II) can also be fabricated by adjusting reactant ratios and reaction temperatures [22,23]. Our previous studies have suggested that manganese minerals with different oxidation states of manganese could be formed when NaClO worked as oxidant.

In this work, pure-phased, $LiMn_2O_4$-mixed and aluminum-doped $LiMnO_2$ cathode materials were hydrothermally fabricated using 0.1 mol L^{-1} $MnCl_2$ and NaClO solutions. Complexant EDTA was used to chelate Mn^{2+} to adjust the reaction rate to obtain single-phased *o*-$LiMnO_2$. The effect of reactant concentration and temperature on the chemical composition of products was studied. The influence of composition and Al doping on the unit cell parameters and the corresponding electrochemical performance of *o*-$LiMnO_2$ was investigated by X-ray diffraction spectrometry, Rietveld structure refinement, Fourier transform infrared spectroscopy, cyclic voltammetry, and electrochemical impedance spectroscopy.

2. Materials and methods

2.1. *Materials and chemicals*

$MnCl_2 \cdot 4H_2O$ (AR, ≥99.0%), ethylene diamine tetraacetic acid tetrasodium salt ($C_{10}H_{12}N_2O_8Na_4 \cdot 4H_2O$, EDTA, AR, ≥40%), $AlCl_3 \cdot 6H_2O$ (AR, ≥97.0%), $LiOH \cdot H_2O$ (AR, >99.0%), anhydrous ethyl alcohol (AR, ≥99.7%) and NaClO solution (AR, available chlorine content ≥5.2%) were all purchased from China National Medicine Group Shanghai Chemical Reagent Company. High purity metallic lithium pellets (99.9%) were supplied by Wuhan Newthree Technology Co. Ltd., China. All reagents used were of analytical grade, unless otherwise noted.

2.2. *Preparation and characterization of o-$LiMnO_2$*

$MnCl_2 \cdot 4H_2O$ (0.989 g) and EDTA (2.262 g) were first dissolved in distilled deionized water (DDW) in a beaker, and NaClO solution (6.717 g) and $LiOH \cdot H_2O$ (1.253 g) were then added to the above solution system. The suspended solution was adjusted to 50 mL by adding DDW and subsequently transferred into a Teflon-lined stainless steel autoclave with a volume of about 100 mL, sealed and maintained at 120, 150, and 180 ^oC, respectively, for 24 h. The concentration of $MnCl_2$, EDTA, LiOH, and NaClO was controlled as 0.1, 0.1, 0.6, and 0.1 mol L^{-1}, respectively. The

suspension was then cooled to room temperature and washed by repeated filtration until the conductivity of filtrate was below 20.0 μS cm^{-1}, and then dried in an oven at 60 ^{o}C for 24 h.

In order to synthesize Al doped *o*-$LiMnO_2$, $AlCl_3 \cdot 6H_2O$ was added to the above reaction system, and the concentration of LiOH and NaClO was slightly changed accordingly. When the concentration of $AlCl_3$ was 0.005, 0.010, 0.015, and 0.020 mol L^{-1}, LiOH concentration was controlled as 0.6, 0.6, 0.6, and 0.8 mol L^{-1}, and NaClO concentration was adjusted as 0.10, 0.11, 0.12, and 0.12 mol L^{-1}, respectively. The as-prepared Al doped $LiMnO_2$ samples were washed and dried as above.

The as-obtained products were identified by X-ray diffraction spectrometry (XRD, Bruker D8 Advance diffractometer with Cu Kα) at a scan rate of 1^{o} min^{-1} with a step of 0.02^{o}. Structure refinement of XRD data was carried out by Rietveld method using TOPAS software (Bruker). The micro-morphologies of samples were characterized by scanning electron microscopy (FE-SEM, JEOL, JSM-6700F) and transmission electron microscopy (TEM, Hitachi-7650). The particle size distribution of the as-obtained samples was analyzed using software ImageJ 1.46 (National Institutes of Health，USA) by SEM images. Fourier transform infrared spectroscopy (FTIR, Nicolet 8700) was carried out using a DTGS detector by making pellets with KBr powder and $LiMnO_2$/KBr mass ratio about 1: 50, and the resolution was set at 4 cm^{-1} with a scan number of 64. BET surface area of $LiMnO_2$ was tested with a Quantachrome Autosorb-1-C automated N_2 gas adsorption system. The concentration of Al and Mn was measured using an inductively coupled plasma atomic emission spectrometry (ICP-AES, Varian Vista-MPX), and further examined by Varian AAS 240FS atomic absorption spectrometer (Varian, Australia).

2.3. *Electrochemical measurements of o-$LiMnO_2$*

The electrochemical characteristics of the synthesized materials were evaluated by galvanostatic charge/discharge using 2032 coin-type cells assembled in an argon-filled glove box, and the

simulated battery test controlled by a battery testing system (Shenzhen Neware Electric Co. Ltd., China). The cathode mixtures consisted of 75 wt.% active materials (including *o*-$LiMnO_2$, a mixture of *o*-$LiMnO_2$ and $LiMn_2O_4$, and Al doped *o*-$LiMnO_2$) dried at 110 ^oC for 12 h, 15 wt.% acetylene black and 10 wt.% polytetrafluoroeythene binder on an aluminum mesh. The anode and reference electrodes were the same lithium foil. The electrolyte was 1 mol L^{-1} $LiClO_4$ in a mixture of EC, DMC, and EMC with equal volume in this work. Celgard 2400 membrane worked as a separator. The charge/discharge cycles were carried out between 4.3 V and 2.4 V (*vs*. Li^+/Li) at a current density of 100 mA g^{-1} at 25±1 ^oC. The cathode foils were characterized by XRD after different cycles of charge/discharge test.

The electrochemical behaviors of active materials including *o*-$LiMnO_2$ and the mixture of *o*-$LiMnO_2$ and $LiMn_2O_4$ were studied by cyclic voltammetry in the above electrolyte at a scan rate of 0.1 mV s^{-1}. Electrochemical impedance spectroscopy (EIS) was used to characterize the interface properties of the modified electrodes. EIS was employed using a 5 mV rms AC perturbation voltage of frequencies ranging from 0.01 Hz to 100 kHz. EIS data were analyzed by fitting to equivalent circuit models using ZSimpWin 3.10 software package (EChem Software). Electrochemical control was achieved by a computer assisted CHI660B electrochemical system (Shanghai Chenhua Instrument Co. Ltd., China).

3. Results

3.1. *The preparation of o-$LiMnO_2$*

Hydrothermal reactions were conducted in different solution systems containing $MnCl_2$, LiOH, EDTA, and NaClO at 120, 150, and 180 ^oC, respectively, for 24 h. As shown in **Fig. 1a**, a mixture of Mn_3O_4 (JCPDS: 01-1127), *o*-$LiMnO_2$ (JCPDS: 86-0352), and Li_2MnO_3 (JCPDS: 73-0152) was formed when 0.08-0.10 mol L^{-1} NaClO was used in the presence of 0.1 mol L^{-1} $MnCl_2$, 0.6 mol L^{-1} LiOH, and 0.1 mol L^{-1} EDTA at 120 ^oC. A mixed phase of birnessite (JCPDS: 87-1749) and Li_2MnO_3 was obtained when the concentration of NaClO was increased to 0.15 mol L^{-1}. That is,

high concentration of NaClO facilitates the formation of high valent manganese oxides. The influence of hydrothermal temperature on the product composition was also investigated. When reaction temperature was increased to 150 ^{o}C, a mixed phase of Mn_3O_4, *o*-$LiMnO_2$, $LiMn_2O_4$ (JCPDS: 88-1026) and Li_2MnO_3 was formed using 0.08 mol L^{-1} NaClO solution as exhibited in **Fig. 1b**. When NaClO concentration was increased to 0.1 mol L^{-1}, a mixture of *o*-$LiMnO_2$ and $LiMn_2O_4$ was formed, which are both active cathode materials for rechargeable lithium batteries [6,7]. Fortunately, when hydrothermal reaction was conducted at 180 ^{o}C, pure-phased *o*-$LiMnO_2$ was achieved if NaClO concentration was kept at 0.10 mol L^{-1}. However, a mixture of *o*-$LiMnO_2$ and Mn_3O_4 was formed in the presence of 0.08 mol L^{-1} NaClO. Moreover, a mixture of *o*-$LiMnO_2$ and $LiMn_2O_4$ was formed when NaClO concentration was further increased to 0.15 and 0.25 mol L^{-1} (**Fig. 1c**). In another word, hydrothermal temperature and enough NaClO supply played critical roles in the formation of pure *o*-$LiMnO_2$.

Decreasing hydrothermal temperature and increasing the concentration of NaClO facilitate the formation of lithium-manganese-oxide compounds with higher-valent manganese. Only when the hydrothermal reaction was conducted by using 0.1 mol L^{-1} NaClO at 180 ^{o}C for 24 h, could pure-phased *o*-$LiMnO_2$ be formed, and it was represented as M_0. When hydrothermal reaction was performed at 150 ^{o}C with the same reagent compositions as above, a mixture of *o*-$LiMnO_2$ and $LiMn_2O_4$ was obtained with *o*-$LiMnO_2$/$LiMn_2O_4$ mass ratio of 2.45: 1 analyzed by XRD (**Fig. 1b**), which was designated as M_m.

Above results suggested that Mn_3O_4 and *o*-$LiMnO_2$ were first formed, and then $LiMn_2O_4$ and Li_2MnO_3 were formed with increasing the concentration of NaClO. Diffraction peak at 18.5^{o}, 2θ, can be assigned to Li_2MnO_3, the common impurity phase in *o*-$LiMnO_2$ materials [5,13-15,24]. Although the diffraction peaks of Li_2MnO_3 and $LiMn_2O_4$ overlap at about 18.5^{o}, the chemical compositions can be identified by other peaks. $LiMn_2O_4$ exhibits a relative strong diffraction peak at 63.8^{o}, which is observed in the XRD patterns of products as shown in **Fig. 1b** and **1c**. Li_2MnO_3 shows a relative weak diffraction peak at 20.8^{o}, however, there is no diffraction peaks at this

diffraction angle in this work. Therefore, it could be safely concluded that a mixture of *o*-$LiMnO_2$ and $LiMn_2O_4$ was formed when 0.1 mol L^{-1} NaClO was used at 150 ^oC (**Fig. 1b**). When hydrothermal reaction was conducted at 180 ^oC by using 0.15 and 0.25 mol L^{-1} NaClO, the diffraction peaks for the impurity phase in *o*-$LiMnO_2$ materials could also be ascribed to $LiMn_2O_4$ (**Fig. 1c**).

The effect of LiOH concentration on the formation process of *o*-$LiMnO_2$ was investigated in hydrothermal system containing 0.1 mol L^{-1} $MnCl_2$, 0.1 mol L^{-1} NaClO, 0.1 mol L^{-1} EDTA at 180 ^oC for 24 h. As shown in **Fig. 1d**, pure-phased Mn_3O_4 was formed when LiOH concentration was controlled as in the range of 0.1-0.2 mol L^{-1}, and a mixture of Mn_3O_4 and *o*-$LiMnO_2$ was formed when LiOH concentration was increased to 0.4 mol L^{-1}. Single-phased *o*-$LiMnO_2$ was formed when LiOH concentration was increased to 0.6 and 0.8 mol L^{-1}.

EDTA affected the reaction process possibly due to the complexation reaction with Mn^{2+}. As for the hydrothermal reaction of 0.1 mol L^{-1} $MnCl_2$, 0.1 mol L^{-1} NaClO, 0.6 mol L^{-1} LiOH at 180 ^oC for 24 h, a mixture *o*-$LiMnO_2$, Mn_3O_4, and Li_2MnO_3 was formed rather than pure-phased *o*-$LiMnO_2$ (**Fig. S1**), indicating a definite necessity of EDTA for the formation of pure-phased *o*-$LiMnO_2$. **Fig. 2a** and **b** show the SEM images of M_0 and M_m, respectively. As a mixture of *o*-$LiMnO_2$ and $LiMn_2O_4$, M_m exhibited a non-uniform size distribution, and the bigger particles were likely due to *o*-$LiMnO_2$ since similar morphologies were observed for the pure-phased *o*-$LiMnO_2$ (**Fig. 2a**).

3.2. *The preparation of aluminum doped o-$LiMnO_2$*

In order to prepare aluminum doped *o*-$LiMnO_2$, $AlCl_3$ was added to the hydrothermal system, in which pure-phased *o*-$LiMnO_2$ (M_0) was formed at 180 ^oC for 24 h. When Al(III)/Mn(II) molar ratio in reaction system was increased, the concentration NaClO and LiOH should be slightly increased to fabricate single-phased aluminum doped *o*-$LiMnO_2$ samples. Single-phased aluminum doped *o*-$LiMnO_2$ samples could be formed when Al/Mn molar ratios in reaction system were controlled as 0, 0.05, 0.10, 0.15, and 0.20 under the following conditions: LiOH concentration was 0.6, 0.6, 0.6,

0.6, and 0.8 mol L^{-1}, and NaClO concentration was 0.1, 0.1, 0.11, 0.12 and 0.12 mol L^{-1}, respectively. Al/Mn molar percent ratios in *o*-$LiMnO_2$ samples were determined to be 0.34, 0.58, 0.91, and 1.22 when Al/Mn molar ratios in hydrothermal system were controlled as 0.05: 1, 0.10: 1, 0.15: 1, and 0.20: 1, respectively. **Fig. S2** shows the XRD patterns of the as-obtained samples, and they were designated as M_3, M_6, M_9 and M_{12} according to Al/Mn molar ratios in doped *o*-$LiMnO_2$ being 0.34, 0.58, 0.91, and 1.22, respectively. It was noted that the Al/Mn molar ratios in *o*-$LiMnO_2$ phase were significantly positively correlated with those in hydrothermal system, and linearly dependent coefficient R^2 was 0.9971. **Fig. 2c-f** shows the SEM images of M_3, M_6, M_9 and M_{12}, and flake-like structures were observed. The content of doped aluminum had no obvious effect on the micro-morphologies of *o*-$LiMnO_2$.

The particle size distribution of the as-obtained samples was further analyzed using software ImageJ as shown in **Fig. S3**. M_m shows a particle distribution range from 50 to 150 nm. M_0 was formed with bigger particles in the range of 100-200 nm owing to the higher hydrothermal temperature. Aluminum doped *o*-$LiMnO_2$ samples exhibit a broad range of particle sizes, which increased with an increase of aluminum content in doped *o*-$LiMnO_2$. The micromorphologies and particle size were further characterized by TEM as shown in **Fig. S4**. After aluminum doping, the particle size slightly increased with an increase in the content of aluminum in *o*-$LiMnO_2$ likely due to that adding $AlCl_3$ changed the complex state of Mn^{2+} for the formation of Mn^{2+} complexes of chlorides, such as $[MnCl_3]^-$, $[MnCl_4]^{2-}$, and $[MnCl_6]^{4-}$. As for the aluminum doped *o*-$LiMnO_2$ powder, the particles had remarkable difference in size, but similar micromorphologies were observed (**Fig. 2** and **Fig. S4**). The influence mechanism of $AlCl_3$ on the micromorphology and particle size of *o*-$LiMnO_2$ needs to be further studied in future.

Fig. 3 illustrates the FTIR spectra of M_0, M_m, M_3, M_6, M_9, and M_{12}. Most of the bands in the low wave-number region of 400-800 cm^{-1} are attributed to the vibrations of MnO_6 octahedra, and they are main fingerprints of *o*-$LiMnO_2$ and $LiMn_2O_4$ [25,26]. The dominant absorption peaks for pure-phased *o*-$LiMnO_2$ (M_0) at 487 and 633 cm^{-1} were assigned to the asymmetry (ν_{as}) and

symmetry stretching modes (ν_s) of Mn-O [4], respectively. A smaller feature at 439 cm^{-1} was likely owing to LiO_6 octahedra [27,28]. Absorption peak at 1636 cm^{-1} was assigned to the adsorbed water molecules. As for $LiMn_2O_4$, the high frequency bands of the FTIR spectra located at 516 and 632 cm^{-1} are attributed to the asymmetric stretching modes of the MnO_6 group [26,28,29]. Doping Al affected the absorption bands for the symmetry stretching of *o*-$LiMnO_2$, and red shifts occurred from 633 cm^{-1} for M_0 to 623, 603, 613, and 617 cm^{-1} for M_3, M_6, M_9, and M_{12}, respectively. The shift for the absorption peak in FTIR spectra is usually associated the change of interatomic distance in crystal structures, and the similar change was observed in high-frequency components in the band of MO_6 vibration around 600 cm^{-1} when Ni was substituted for cobalt in $LiCoO_2$ [30].

Table 1 shows cell parameters obtained by Rietveld structure refinement, and specific surface area (SSA) for M_0, M_m, M_3, M_6, M_9, and M_{12}. As the content of doped Al in *o*-$LiMnO_2$ increasing, parameter *a* decreased, while *b* increased. Moreover, parameter *c* was first slightly decreased and then increased, and cell volume slightly shrinked with increasing the content of doped aluminum due to that Al^{3+} ionic radius (0.0535 nm) is smaller than that of Mn^{3+} (0.0645 nm) [5,31]. The most significant decrease along *a* axis occurred after substitution, which would possibly improve the electrochemical stability due to that the Jahn-Teller distortion of the [$Mn^{3+}O_6$] octahedra induces an elongation along the *a* direction [5].

It should be pointed out that these experiments have been repeated more than three times for that sufficient active materials should be supplied for the characterization of electrochemical performance. The as-prepared powder samples were characterized by XRD and FTIR each time, and same results were obtained. The SEM images also showed the uniform morphologies, which further suggested that the pure products were synthesized. The composition of Al doped *o*-$LiMnO_2$ was also analyzed by Varian AAS 240FS atomic absorption spectrometer (Varian, Australia), besides the ICP-AES as mentioned above. That was to say, the composition of Al doped *o*-$LiMnO_2$ was confirmed by two analysis techniques, further suggesting that the experiments were repeatable.

3.3. *The electrochemical performance of o-$LiMnO_2$*

Fig. 4 shows discharge specific capacity and cyclic stability of M_0, M_3, M_6, M_9, M_{12}, and M_m at a current density of 100 mA g^{-1}. M_0 had a relatively low initial discharge specific capacity of 76 mAh g^{-1}, and increased to about 139 mAh g^{-1} after 25 cycles. The cyclic capacity was kept stable, and discharge specific capacity was about 124 mAh g^{-1} after 100 cycles. Among the as-obtained samples, M_m showed the largest discharge specific capacity. The initial discharge capacity of M_m was 139 mAh g^{-1}, and increased to 171 mAh g^{-1} after 25 cycles, and retained about 144 mAh g^{-1} after 100 cycles. As reported, a mixture of $LiMnO_2$ and Li_2MnO_3 with mass ratio of 1.40: 1 exhibited the best electrochemical performance [32]. In this work, the mixture of *o*-$LiMnO_2$ and $LiMn_2O_4$ with *o*-$LiMnO_2$/$LiMn_2O_4$ mass ratio about 2.45: 1 exhibited excellent electrochemical performance.

Doping aluminum improved the electrochemical performance of *o*-$LiMnO_2$ as displayed in **Fig. 4**. The discharge capacity increased at the initial few cycles and then kept steady after 25 cycles. The increase of discharge capacity in the first few cycles was likely due to the electrochemical activation of cathode materials and the improvement of lithium ion diffusion channels in active materials, resulting in higher lithium utilization during initial cycling stage.The cyclic capacity of doped *o*-$LiMnO_2$ was first increased and then decreased with an increase in the content of aluminum. The initial discharge capacity of M_6 was 82 mAh g^{-1}, and kept steady at about 160 mAh g^{-1} after 25 cycles, and slightly decreased to 156 mAh g^{-1} after 100 cycles. The as-obtained *o*-$LiMnO_2$ samples exhibited better electrochemical performance than those synthesized by other methods [5,7,33].

Intermediate products in charge/discharge processes were studied using XRD after different cycles. As illustrated in **Fig. 5a**, a mixed phase of *o*-$LiMnO_2$ and $LiMn_2O_4$ was formed after charge/discharge test of the first cycle. *o*-$LiMnO_2$ was almost completely transformed into $LiMn_2O_4$ after five cycles, and a mixture of $LiMn_2O_4$, monoclinic $LiMnO_2$ (*m*-$LiMnO_2$, JCPDS: 87-1255) and γ-MnO_2 was formed after 100 cycles. The similar results were obtained for the aluminum doped

o-$LiMnO_2$ sample of M_6 after 100 cycles as shown in **Fig. 5b**. $Li_2Mn_2O_4$ (JCPDS: 84-1523) was also formed in this process. As reported, *o*-$LiMnO_2$ was converted to other manganese oxides, such as $Li_xMn_2O_4$ [7,33,34], which was then gradually transformed into *m*-$LiMnO_2$ and MnO_2 [35]. In this work, similar intermediate products were also observed.

Electrochemical impedance spectroscopy was collected to analyze the change trend of electrical conductivity and ionic migration rate. The semicircle at the high frequency region was related to the solid electrolyte interface film of the newly assembled cell. The curve at low frequency region can be explained as the diffusion-controlled process in the electrolytes. **Fig. 6** shows the typical families of Nyquist plots obtained from electrodes of M_0, M_m, M_3, M_6, M_9, and M_{12} and measured using 3.15 V of open circuit voltage at 25 ^oC before charge/discharge test. The particle size, morphologies and specific surface area of the above samples were similar as shown in **Fig. 2**, **Fig. S3**, and **Table 1**, and the same electrochemical reaction mode R(QR)WC was used to compare their reaction impedance (R_{ct}) and lithium ion diffusion rates in this work [36]. As shown in **Table 2**, R_{ct} of M_m was higher than that of M_0. It was found that doping aluminum improved conductivity and the corresponding R_{ct} was decreased. A Warburg type element in the low frequency region corresponded to solid-state diffusion of lithium ions and a steep line at the lower frequencies. Diffusion rate of lithium ions in solid phase could be reflected by the linear slope in the low frequency region, and the Z_w values for all the samples were compared as shown in **Table 2**. As for M_0, M_3, M_6, M_9, and M_{12}, the diffusion rate of lithium ions increased with a decrease in the cell volume of Al doped *o*-$LiMnO_2$.

4. Discussion

4.1. *The influence on o-$LiMnO_2$ formation process*

Hydrothermal reactions have been widely conducted to synthesize *o*-$LiMnO_2$ from different low-valent manganese oxide precursors including Mn_3O_4, Mn_2O_3 and MnOOH, whose micro-morphologies could possibly be preserved during the transformation of target products

[3,10,14,17,20,24]. In the present work, Mn_3O_4 was found to be one of the intermediate products in the formation process of *o*-$LiMnO_2$. When the concentrations of $MnCl_2$, LiOH, and EDTA were controlled as 0.1, 0.6, and 0.1 mol L^{-1}, respectively, Mn_3O_4 was first formed, and then oxidized to Li_2MnO_3 and birnessite-type manganese oxides with increasing the concentration of NaClO at 120 ^oC (**Fig. 1a**). The formation of layered birnessite was attributed to the high concentration of Na^+, which participated in the reaction and intercalated into the interlayer to support the layered structure. When hydrothermal temperature was increased to 150 ^oC, the content of Li_2MnO_3 in solid products increased with increasing the concentration of NaClO (**Fig. 1b**). Li_2MnO_3 was formed and transformed into $LiMnO_2$ at a higher hydrothermal temperature [15,21]. Birnessite was not formed likely due to the formation of Li_2MnO_3 and $LiMn_2O_4$ at 150 ^oC [21]. These results suggested that birnessite could be used as precursor to prepare nano-sized Li_2MnO_3, $LiMn_2O_4$ and $LiMnO_2$ with various morphologies because the morphologies and particle size of birnessite could be controlled easily as reported in our previous work [37]. The transformation of $LiMnO_2$ was a complicated multi-step process, and influencing factors included hydrothermal temperature, LiOH concentration, the additives of organics and cation, *etc*.

Hydrothermal temperature plays an important role in the formation of $LiMnO_2$. Different temperatures were needed when Mn_3O_4, Mn_2O_3 and MnOOH worked as precursors. For example, $LiMnO_2$ samples were hydrothermally synthesized using Mn_2O_3 precursor at 150 ^oC [20]，160 ^oC [10,14,24] and 170 ^oC [17]. When MnOOH was used instead, the hydrothermal reaction was conducted at 200 ^oC [3]. In the case of Mn_3O_4 used as a precursor, hydrothermal treatment was performed with high concentration of LiOH at 170 ^oC for 4 d [38]. Hydrothermal temperature was somewhat higher when Mn_3O_4 was used likely due to its lower reaction activity than that of Mn_2O_3, and oxidant was needed to prepare *o*-$LiMnO_2$. In this work, pure-phased *o*-$LiMnO_2$ was formed by adding oxidant NaClO at 180 ^oC for 24 h. Hydrothermal temperature should be elevated to synthesize the target product of *o*-$LiMnO_2$ possibly due to the further redox reactions between organics and manganese oxides, such as birnessite, Li_2MnO_3 and $LiMn_2O_4$ [39].

In order to save raw materials and manufacturing cost, the dosage of LiOH was concerned in the preparation process of $LiMnO_2$. Only Mn_3O_4 was formed when LiOH of low concentration ($\leq$ 0.2 mol L^{-1}) was used, and a mixture of Mn_3O_4 and $LiMnO_2$ was formed when LiOH was 0.4 mol L^{-1}. Pure-phased target product was formed when 0.6 mol L^{-1} LiOH was used, and crystallinity was increased when 0.8 mol L^{-1} LiOH was used instead (**Fig. 1d**). LiOH was reacted with Mn_3O_4 and Mn_2O_3 to form *o*-$LiMnO_2$, and high concentration reactant facilitated this transformation process [17,24,38]. High concentration of LiOH was usually supplied to fabricate *o*-$LiMnO_2$ when low-valent manganese oxides were used as precursor for hydrothermal reaction. It was possible due to that water molecules were produced during the formation of *o*-$LiMnO_2$, which reduced the formation rate of the *o*-$LiMnO_2$ phase and increased the reaction time [17], particularly for the mass transport of Li^+ in the pores of manganese oxides during the hydrothermal process. As for the one-step synthesis of $LiMnO_2$, a mixture of $LiMnO_2$ and Li_2MnO_3 was formed when LiOH/$MnSO_4$ molar ratio was less than 4: 1 [21]. Although Li/Mn molar ratio was increased to 30, the final product was a *o*-$LiMnO_2$ crystalline phase with trace amounts of Li_2MnO_3 [15], and the mixture was also observed as intermediate product in this work (**Fig. 1a** and **b**). The rapid generation of manganese oxides was unfavorable to the formation of target product due to that big crystal particle would inhibit the further reaction. As reported, $LiMnO_2$ crystal grain would not be formed when hydrothermal temperature was too high [24]. High concentration of Li^+ facilitated the formation of *o*-$LiMnO_2$ mostly due to an increase in Li^+ mobility, which accelerated its reaction with Mn(III/II) source to form lithium manganese oxides, and was also beneficial to the formation of a layered structure. In the present work, Li/Mn molar ratio could be controlled as 6: 1, which was lower than those as reported [3,15,24]. Low concentration of Li^+ was performed to reduce cost, and complexation reaction resulted in a slow crystallization process and decreased the negative influence of low mass transfer rate of Li^+ on the formation of *o*-$LiMnO_2$. When EDTA was not added to the reaction system, pure phased $LiMnO_2$ was not formed, and a mixed phase of *o*-$LiMnO_2$, Mn_3O_4, and Li_2MnO_3 was generated instead (**Fig. S1**). The formation rate of manganese oxides

would be remarkably decreased due to the complexation reaction of EDTA and Mn^{2+} before hydrothermal reaction. As reported in our previous work, rapid transformation from $Mn(OH)_2$ precipitate to Mn_3O_4 occurred in air [40]. However, Mn_3O_4 was not formed in alkali solution after adding EDTA into the hydrothermal system in the present work. The formation rate of manganese oxides would be remarkably decreased due to the formation of the Mn^{2+} complexes of EDTA before hydrothermal reaction. The formation of complexes by adding organics tetrabutylammonium bromide and tetraoctylammonium bromide into $MnSO_4$ solution could prevent its rapid reaction with $KMnO_4$ to form cryptomelane-type manganese oxides with different degrees of crystallinity [39]. $LiMnO_2$ was formed with Li/Mn molar ratio as low as 1.05 when Mn_2O_3 precursor was used in miscible solvents with a low reaction rate [17]. In order to further reduce cost, some cheaper complexant would be used to substitute EDTA in future work.

The addition of $AlCl_3$ consumed OH^- to form AlO_2^-, and also affected the oxidation capacity of NaClO in strong alkaline solution systems [22,23]. The preparation of doped *o*-$LiMnO_2$ by one-step hydrothermal synthesis was seldom reported, which was likely due to the precipitation reaction of metal cations and hydroxide ions. In this work, soluble AlO_2^- was formed using $AlCl_3$ in LiOH solution of high concentration. In order to adjust the alkalinity and oxidation capacity of NaClO, the concentrations of LiOH and NaClO were slightly increased when $AlCl_3$ concentration was increased. LiOH concentrations were controlled as 0.6, 0.6, 0.6, 0.6, and 0.8 mol L^{-1}, and NaClO concentrations were controlled as 0.1, 0.1, 0.11, 0.12, and 0.12 mol L^{-1}, when Al/Mn molar ratios in reaction system were controlled as 0, 0.05, 0.10, 0.15, and 0.20, respectively. When the concentrations of LiOH and NaClO were not adjusted accordingly, a mixture of Mn_3O_4 and *o*-$LiMnO_2$ with a small amount of $LiMn_2O_4$ was formed (figure not given). It should be pointed out that Al/Mn molar percent ratios in *o*-$LiMnO_2$ phase were only 0.34, 0.58, 0.91, and 1.22 when Al/Mn molar ratios in reaction system were controlled as 0.05: 1, 0.10: 1, 0.15: 1, and 0.20: 1, respectively. The formation of anion AlO_2^- did not well facilitate the formation of doped $LiMnO_2$

with high content of Al^{3+} ions. The detailed reaction processes and influence mechanisms are currently underway.

4.2. *The effect on o-$LiMnO_2$ electrochemical performance*

Chemical composition, crystal structure, crystallinity and cell parameters possibly affected the electrochemical performance of active electrode materials. The cyclic voltammetric behavior of M_0 and M_m was studied after two cycles of charge/discharge activation. As shown in **Fig. 7**, oxidation/reduction current peaks A/A' (3.9 V) and B/B' (4.1 V) were associated with the reversible deinsertion/insertion processes of lithium ion between $LiMn_2O_4$ and MnO_2, and a pair of peaks C/C' (3.2 V/2.7 V) corresponded to the insertion/extraction of lithium between cubic $LiMn_2O_4$ and tetragonal $Li_2Mn_2O_4$ [5,41], and these intermediate products could be determined (**Fig. 5**). More than 50% Jahn-Teller ions (Mn^{3+}) presented in $Li_2Mn_2O_4$ participated in the transformation process of cubic $LiMn_2O_4$ to tetragonal $Li_2Mn_2O_4$, and the phase transformation results in the volume shrinkage of unit cell that imparts a high degree a stress in grains. Grain fracture may occur with the repeating insertion/extraction of Li^+ in this process, which finally results in the capacity loss [9,41]. The reduction current peak intensity of M_m was stronger than that of M_0 likely due to the participation of $LiMn_2O_4$ in M_m, which worked as an intermediate product after a few charge/discharge cycles (**Fig. 5**). The discharge capacity of M_m was higher than that of M_0 because the former needed not to be activated in the initial stage (**Fig. 4**). Small particle size and large specific surface area facilitate the high electrochemical performance of $LiMnO_2$ and $LiMn_2O_4$ cathode materials [13,42]. It was noted that the specific surface area of M_m was about 21.3 m^2 g^{-1}, two times larger than that of M_0 (9.1 m^2 g^{-1}), and it may lead to a better electrochemical performance. As a fact, the as-obtained *o*-$LiMnO_2$ would be oxidized and transformed into $LiMn_2O_4$ through heat-treatment at 300-600 ^oC in air for 2 h (**Fig. S5**). $LiMn_2O_4$, M_{600}, from the transformation of *o*-$LiMnO_2$ using heat treatment at 600 ^oC with specific surface area about 12.6 m^2 g^{-1}, exhibited an initial discharge capacity of 134 mAh g^{-1}, and kept steady at about 120 mAh g^{-1}

after 20 cycles, and decreased to 117 mAh g^{-1} after 100 cycles (**Fig. S6**). The decrease of electrochemical performance further indicated the influence of specific surface area. Specific surface area, particle size, and theoretical specific capacity all affect the electrochemical lithium storage performance. Mixing *o*-$LiMnO_2$ also improved the electrochemical performance of $LiMn_2O_4$ in the present work. Therefore, forming a mixed phase of $LiMn_2O_4$ and *o*-$LiMnO_2$ would improve the electrochemical performance of single *o*-$LiMnO_2$ and $LiMn_2O_4$, which was another highlight of this work.

The influence of cell parameters on the electrochemical performance of $LiMnO_2$ was further analyzed by discharge/charge profiles at a current density of 100 mA g^{-1}. A remarkable discharge voltage plateau at 3.3-2.4 V was observed for pure-phased M_0 (**Fig. 8**). Plateau at 3.3-2.4 V was owing to the discharge of orthorhombic $LiMnO_2$ or tetragonal $Li_2Mn_2O_4$ [3,4]. A new voltage plateau at 4.3-3.6 V was formed and kept stable after 20 cycles, likely due to the formation of spinel $LiMn_2O_4$, which was further transformed into tetragonal $Li_2Mn_2O_4$ (**Fig. 5**), and $Li_xMn_2O_4$ ($0<x<2$) was also could be formed [4,7,20,35,41]. The discharge capacity increased with an increase in the cyclic number during the charge/discharge test, and kept stable after 20 cycles likely due to the activation process [3]. After 100 cycles, the discharge voltage at 4.3-3.6 V was remarkably lowered for M_0 and M_m possibly due to the disproportionation of $Li_2Mn_2O_4$ to Mn^{2+} and MnO_2, resulting in capacity fade [35,41,43]. However, there is no obvious change for the discharge plateau of M_6 (**Fig. 8c**), which was attributed to that aluminum doping affected the crystal lattice and electrochemical performance of $LiMnO_2$ [5]. The Jahn-Teller distortion of the [$Mn^{3+}O_6$] octahedra induces an elongation along the *a* direction [5]. However, parameter *a* decreased with an increase in the content of doped Al in $LiMnO_2$ (**Table 1**). The distorted axial Mn^{3+}-O bond length of 0.229 nm is greater than the typical Al^{3+}-O bond length (0.19 nm) in octahedral coordination [5], and the most significant changes due to substitution were expected to occur along *a* axis. These changes inhibited the shrinkage distortion during charge/discharge process, and excellent cyclic stability was achieved [4,5,44]. In this work, appropriate content of doped aluminum with Al/Mn molar percent ratio about

0.58 exhibited the best electrochemical performance. It should be pointed out that the appropriate decrease in cell volume with compression along *a* axis and stretch along *b* axis facilitated the cyclic stability of *o*-$LiMnO_2$ by Al doping due to the shrinkage of cell volume for the formation of $LiMn_2O_4$ during the charge/discharge process [31]. However, an increase in cell volume facilitated the electrochemical stability of $LiMn_2O_4$ owing to the expansion of cell volume for the formation of $Li_2Mn_2O_4$ during the charge/discharge process [44,45]. Aluminum doping decreases Jahn-Teller distortion and improves the cyclic stability due to that the phase transformation from *o*-$LiMnO_2$ to $LiMn_2O_4$ occurs in the charge/discharge test. In this work, although $LiMn_2O_4$ was formed as an intermediate product during the charge/discharge test, the discharge capacity of *o*-$LiMnO_2$ was about 160 mAh g^{-1}, which was much higher than that of $LiMn_2O_4$ [4,5,7-9].

During the charge/discharge processes, lithium ions migrate out of the lattice along *c* axis, and oxygen position does not change with Li^+ extraction, resulting in the formation of vacant octahedral sites [43,46]. Subsequently, half of the manganese ions migrate statistically into the vacant octahedral sites along *b* axis, and the migration of metal ions is accompanied by a slight shift for oxygen atoms to the ideal cubic closest packing positions with cubic symmetry [9,46,47]. From the results of FTIR (**Fig. 3**) and Rietveld refinement (**Table 1**), it could be concluded that the bond energy of Mn-O towards the equatorial plane of MnO_6 octahedron was lowest in M_6, which facilitated the migration of manganese ions into the vacant octahedral sites [46,47]. The transformation of *o*-$LiMnO_2$ to spinel $LiMn_2O_4$ easily occurred in the initial stage of charge/discharge test (**Fig. 5a**). To a certain degree, electrochemical reaction impedance in the initial stage positively correlated with the difficulty of phase change. In this work, M_6 had the lowest reaction impedance before charge/discharge test (**Fig. 6**, **Table 2**). Phase transformation easily occurred in the electrochemical process, and exhibited stable electrochemical lithium storage performance after activation of a few cycles.

As for the charge processes of M_0, pure-phased $LiMnO_2$, a short charging voltage plateau at about 3.15 V was observed at the first cycle. The similar results were also reported in the literature

[5,7,14]. The presence of the short charge plateau was possibly due to the activation of *o*-$LiMnO_2$ and the formation of $LiMn_2O_4$ in this process. As seen from the multi-cycle charge curves of M_0 and M_6, voltage plateau at about 3.15 V was extended due to the increase of the content of $LiMn_2O_4$ formed in charge/discharge test [9]. As for M_m, this charge plateau was more obvious after charge/discharge activation of five cycles for the high content of $LiMn_2O_4$ in cathode materials (**Fig. 8b**). These results were consistent with the cyclic voltammograms as shown in **Fig. 7**. The formation of $LiMn_2O_4$ could be further confirmed by the XRD analysis of electrode materials as illustrated in **Fig. 5** after charge/discharge test of the first cycle. To further improve the electrochemical cyclic stability of *o*-$LiMnO_2$, the phase transition from layered to spinel structure might be remarkably retarded by doping other metal ions, such as Ni [19]. This hydrothermal method also provides the possibility for the preparation of other metal doped *o*-$LiMnO_2$.

Decreasing reaction impedance (R_{ct}) may effectively improve the electrochemical performance of *o*-$LiMnO_2$ and $LiMn_2O_4$ cathode materials. As seen in **Fig. 6**, the R_{ct} values of the as-obtained samples were greater than 200 Ω. In order to improve the electrochemical performance, carbon materials, such as carbon nanotube and graphene, modified *o*-$LiMnO_2$ might be directly synthesized using this hydrothermal system, and this study is currently underway.

5. Conclusions

Pure-phased, $LiMn_2O_4$-mixed, and aluminum-doped *o*-$LiMnO_2$ cathode materials of rechargeable lithium batteries with high discharge capacity and excellent cyclic stability have been successfully fabricated using Mn(II) salt by a facile one-step hydrothermal treatment at 180 ^oC for 24 h. The molar ratio of Li^+/Mn^{2+} can be controlled as low as 6, and the complexation reaction of EDTA and Mn^{2+} facilitates the formation of *o*-$LiMnO_2$. Al/Mn molar percent ratio in aluminum-doped $LiMnO_2$ is in the range of 0 to 1.22 when $AlCl_3/MnCl_2$ molar ratio is controlled from 0 to 20% in reaction system. LiOH and NaClO concentration should be slightly increased to obtain single-phased aluminum-doped *o*-$LiMnO_2$ when Al/Mn molar ratio increased in hydrothermal system. Mixing

$LiMn_2O_4$ and doping aluminum improve the electrochemical lithium storage capacity and cyclic stability of *o*-$LiMnO_2$. Aluminum doped $LiMnO_2$ with Al/Mn molar percent ratio of 0.58 shows the best electrochemical performance. Pure-phased *o*-$LiMnO_2$, a mixture of *o*-$LiMnO_2$ and $LiMn_2O_4$ ($LiMnO_2$/$LiMn_2O_4$ mass ratio = 2.45: 1), and aluminum doped $LiMnO_2$ (Al/Mn molar ratio = 0.58%) exhibits the initial discharge capacity of 76.0, 139.1 and 81.8 mAh g^{-1}, and cycling capacity of 124.1, 143.7and 155.8 mAh g^{-1} after 100 cycles, respectively. This preparation method and the study on the electrochemical properties widen the potential application of pure-phased and doped *o*-$LiMnO_2$ in the field of rechargeable lithium-ion battery.

Acknowledgments

The authors thank the National Natural Science Foundation of China (Grant Nos.: 41171375 and 20807019), the Program for New Century Excellent Talents in University of China (No. NCET-12-0862), the Young Outstanding Talent Foundation of Hubei Province of China (No. 2012FFA031), and the Fundamental Research Funds for the Central Universities (Program No.: 2013PY029, 2013PY030, 2011PY015, 2009SC007 and 2012SC31,) for financial support. The authors also gratefully acknowledge Dr. Wenfeng Tan at Huazhong Agricultural University and Dr. Xiaoqing Qiu at Fuzhou University for useful suggestions.

Reference

[1] M. Armand, J.-M. Tarascon, *Nature*, 2008, **451**, 652-657.

[2] H. Nishide, K. Oyaizu, *Science*, 2008, **319**, 737-738.

[3] X. L. Xiao, L. Wang, D. S. Wang, X. M. He, Q. Peng, Y. D. Li, *Nano Res*., 2009, **2**, 923-930.

[4] C. Liu, J. M. Nan, X. X. Zuo, X. Xiao, D. Shu, *Int. J. Electrochem. Sci*., 2012, **7**, 7152-7164.

[5] J. B. Cook, C. Kim, L. P. Xu, J. Cabana, *J. Electrochem. Soc*., 2013, **160**, A46-A52.

[6] J. B. Goodenough, Y. Kim, *Chem. Mater*., 2010, **2**, 587-603.

[7] P. G. Bruce, A. R. Armstrong, R. L. Gitzendanner, *J. Mater. Chem*., 1999, **9**, 193-198.

[8] J. Cho, Y. J. Kim, T.-J. Kim, B. Park, *Chem. Mater*., 2001, **13**, 18-20.

[9] Y.-Il. Jang, B. Y. Huang, H. F. Wang, D. R. Sadoway, Y.-M. Chiang, *J. Electrochem. Soc.*, 1999, **146**, 3217-3223.

[10] H. Xu, J. Sun, L. Gao, *Ionics*, 2013, **19**, 63-69.

[11] Z. P. Guo, S. Zhong, G. X. Wang, H. K. Liu, S. X. Dou, *J. Alloy. Compd*., 2003, **348**, 231-235.

[12] G. Ceder, S. K. Mishra, *Electrochem. Solid-State Lett.*, 1999, **2**, 550-552.

[13] Z. P. Guo, K. Konstantinov, G. X. Wang, H. K. Liu, S. X. Dou, *J. Power Sources*, 2003, **119-121**, 221-225.

[14] H. M. Ji, G. Yang, X. W. Miao, A. Q. Hong, *Electrochim. Acta*, 2010, **55**, 3392-3397.

[15] J. L. Xie, X. Huang, Z. B. Zhu, J. H. Dai, *Ceram. Int*., 2011, **37**, 419-421.

[16] R. I. Walton, *Chem. Soc. Rev*., 2002, **31**, 230-238.

[17] Y. He, Q. Feng, S. Q. Zhang, Q. L. Zou, X. L. Wu, X. J. Yang, *ACS Sustainable Chem. Eng*. 2013, **1**, 570-573.

[18] Z. P. Guo, G. X. Wang, H. K. Liu, S. X. Dou, *Solid State Ionics*, 2002, **148**, 359-366.

[19] K. S. Park, M. H. Cho, S. H. Park, K. S. Nahm, Y. K. Sun, Y. S. Lee, M. Yoshio, *Electrochim. Acta*, 2002, **47**, 2937-2942.

[20] Z. Su, Z. W. Lu, X. P. Gao, P. W. Shen, X. J. Liu, J. Q. Wang, *J. Power Sources*, 2009, **189**, 411-415.

[21] X. K. Huang, Q. S. Zhang, H. T. Chang, J. L. Gan, H. J. Yue, Y. Yang, *J. Electrochem. Soc.*, 2009, **156**, A162-A168.

[22] G. H. Qiu, J. Wang, W. Zhao, X. H. Feng, W. F. Tan, Q. Zhang, F. Liu, *Chin. J. Chem*., 2010, **28**, 2301-2307.

[23] H. Yin, F. Liu, X. H. Chen, X. H. Feng, W. F. Tan, G. H. Qiu, *Micropor. Mesopor. Mater*., 2012, **153**, 115-123.

[24] Q. Liu, Y. X. Li, Z. L. Hu, D. L. Mao, C. K. Chang, F. Q. Huang, *Electrochim. Acta*, 2008, **53**, 7298-7302.

[25] R. Chitrakar, K. Sakane, A. Umeno, S. Kasaishi, N. Takagi, K. Ooi, *J. Solid State Chem*., 2002, **169**, 66-74.

[26] Y. M. Hon, S. P. Lin, K. Z. Fung, M. H. Hon, *J. Eur. Ceram. Soc*., 2002, **22**, 653-660.

[27] L. A. Riley, S. V. Atta, A. S. Cavanagh, Y. F. Yan, S. M. George, P. Liu, A. C. Dillon, S.-H. Lee, *J. Power Sources*, 2011, **196**, 3317-3324.

[28] S. Chitra, P. Kalyani, T. Mohan, R. Gangadharan, B. Yebka, S. Castro-Garcia, M. Massot, C. Julien, M. Eddrief, *J. Electroceram*., 1999, **3**, 433-441.

[29] C. Wu, Z. X. Wang, F. Wu, L. Q. Chen, X. J. Huang, *Solid State Ionics*, 2001, **144**, 277-285.

[30] D. Ostrovskii, F. Ronci, B. Scrosati, P. Jacobsson, *J. Power Sources*, 2001, **94**, 183-188.

[31] W.-H. Ryu, J.-Y. Eom, R.-Z. Yin, D.-W. Han, W.-K. Kim, H.-S. Kwon, *J. Mater. Chem*., 2011, **21**, 15337-15342.

[32] G. Yang, H. M. Ji, P. Gao, A. Q. Hong, H. R. Ding, S. Roy, J. Pinto, X. F. Jiang, *J. Electrochem. Soc.*, 2011, **158**, A1071-A1078.

[33] Y.-J. Gu, Y.-B. Chen, H.-K. Wu, Y.-M. Wang, L. Chen, M. Wang, X.-W. Huang, H. Zheng, X.-B. Liu, Ch. Lu, Y. Hu, *Energy Materials*, 2009, **4**, 40-43.

[34] C.-H. Lu, H.-C. Wang, *J. Eur. Ceram. Soc*., 2004, **24**, 717-726.

[35] J. Cho, T.-J. Kim, B. Park, *J. Electrochem. Soc.*, 2002, **149**, A288-A292.

[36] L. L. Xiong, Y. L. Xu, C. Zheng, Z. W. Zhang, J. B. Li, *J. Solid State Electrochem*., 2011, **15**, 1263-1269.

[37] H. J. Cui, G. H. Qiu, X. H. Feng, W. F. Tan, F. Liu, *Clay Clay Miner*., 2009, **57**, 715-724.

[38] S.-T. Myung, S. Komaba, N. Kumagai, *Electrochim. Acta*, 2002, **47**, 3287-3295.

[39] G. H. Qiu, H. Huang, S. Dharmarathna, E. Benbow, L. Stafford, S. L. Suib, *Chem. Mater*., 2011, **23**, 3892-3901.

[40] Q. H. Qiu, Q. Li, Y. Yu, X. H. Feng, W. F. Tan, F. Liu, *J. Soil. Sediment.*, 2011, **11**, 1323-1333.

[41] S. B. Tang, M. O. Lai, L. Lu, *J. Power Sources*, 2007, **164**, 372-378.

[42] Y. C. Chen, K. Xie, Y. Pan, C. M. Zheng, *J. Power Sources*, 2011, **196**, 6493-6497.

[43] J. Cho, M. M. Thackeray, *J. Electrochem. Soc.*, 1999, **146**, 3577-3581.

[44] Y. Shin, A. Manthiram, *Chem. Mater.*, 2003, **15**, 2954-2961.

[45] Y. Shin, A. Manthiram, *J. Electrochem. Soc.*, 2004, **151**, A204-A208.

[46] W. P. Tang, H. Kanoh, K. Ooi, *J. Solid State Chem.*, 1999, **142**, 19-28.

[47] J. Akimoto, Y. Takahashi, Y. Gotoh, K. Kawaguchi, K. Dokko, I. Uchida, *Chem. Mater.*, 2003, **15**, 2984-2990.

Tables

Table 1 Cell parameters and specific surface area (SSA) of the as-obtained samples.

Samples	*a* (nm)	*b* (nm)	*c* (nm)	Cell volume (nm^3)	R_{wp} (%)	SSA ($m^2\ g^{-1}$)	Al/Mn molar ratio (%)
M_0	0.4577	0.5751	0.2811	0.07398	12.6	9.1	0
M_m	/	/	/	/	/	21.3	/
M_3	0.4569	0.5756	0.2811	0.07392	13.5	9.7	0. 34
M_6	0.4561	0.5759	0.2810	0.07383	13.6	10.2	0. 58
M_9	0.4548	0.5764	0.2813	0.07373	14.7	10.6	0. 91
M_{12}	0.4542	0.5764	0.2812	0.07362	13.5	13.5	1.22

Table 2 EIS model (R(QR)WC) parameters for M_0, M_m, M_3, M_6, M_9 and M_{12} before discharge/charge tests.

Samples	M_0	M_m	M_3	M_6	M_9	M_{12}
R_{ct} (Ω)	229.4	297.9	176.1	145.0	252.5	203.0
Error (%)	1.246	0.935	0.779	0.913	1.357	0.982
Z_w ($S/s^{1/2}$)	0.011	0.009	0.015	0.015	0.007	0.009
Error (%)	5.387	3.685	3.663	3.559	5.111	3.173

Figure captions

Fig. 1. XRD patterns of products synthesized in hydrothermal systems containing 0.1 mol L^{-1} $MnCl_2$, 0.1 mol L^{-1} EDTA, LiOH and NaClO for 24 h: 0.6 mol/L LiOH with different concentration of NaClO at 120 ^oC (a), 150 ^oC (b), and 180 ^oC (c); 0.1 mol/L NaClO with different concentration of LiOH at 180 ^oC (d).

Fig. 2. SEM images of M_0 (a), M_m (b), M_3 (c), M_6 (d), M_9 (e) and M_{12} (f).

Fig. 3. FTIR spectra of M_0, M_m, M_3, M_6, M_9, and M_{12}.

Fig. 4. Discharge specific capacity *vs*. cycle number at the current density of 100 mA g^{-1} for M_0, M_3, M_6, M_9, M_{12}, and M_m after heat-treatment at 110 ^oC for 12 h.

Fig. 5. XRD patterns of intermediate products after different cycles of charge/discharge test for M_0 (a), and 100 cycles of charge/discharge test for M_0 and M_6 (b).

Fig. 6. Electrochemical impedance spectra of M_0, M_3, M_6, M_9, M_{12}, and M_m as Nyquist plots measured at 25 ^oC before charge/discharge test.

Fig. 7. Cyclic voltammograms of M_0 and M_m in 1.0 mol L^{-1} $LiClO_4$ +EC+DMC+EMC with equal volume within potential range of 2.0-4.3 V (*vs*. Li/Li^+) with a scan rate of 0.1 mV s^{-1}.

Fig. 8. Discharge/recharge profiles of M_0 (a), M_m (b), and M_6 (c) for different cycles at a current density of 100 mA g^{-1}.

Figures

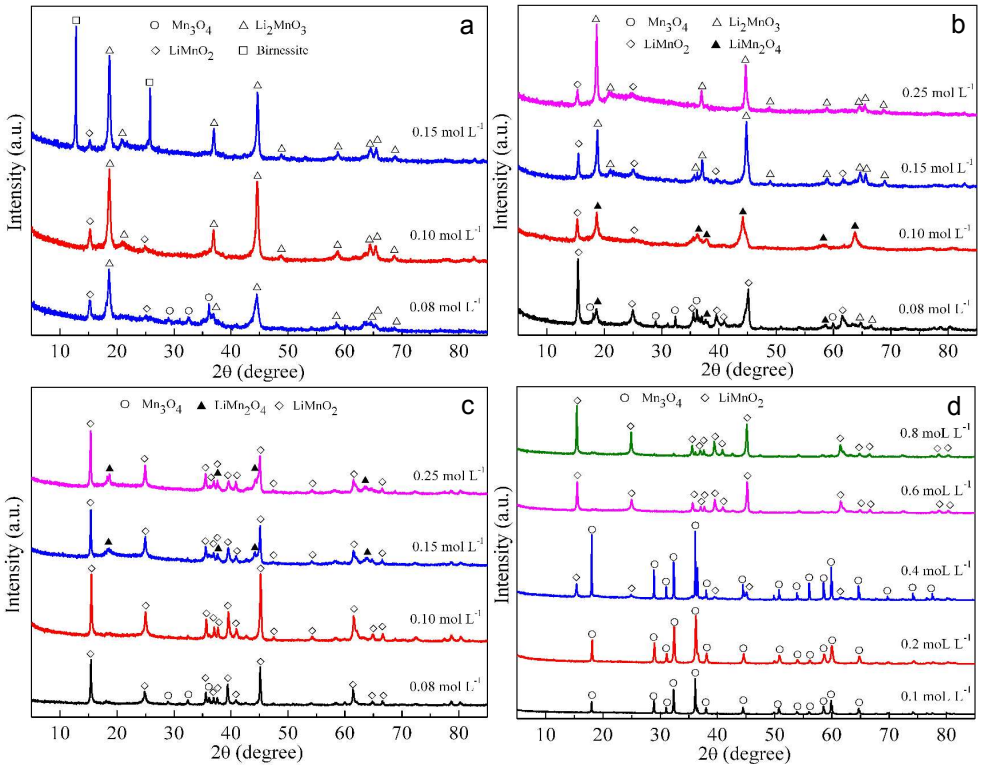

Fig. 1. XRD patterns of products synthesized in hydrothermal systems containing 0.1 mol L^{-1} $MnCl_2$, 0.1 mol L^{-1} EDTA, LiOH and NaClO for 24 h: 0.6 mol/L LiOH with different concentration of NaClO at 120 ^oC (a), 150 ^oC (b), and 180 ^oC (c); 0.1 mol/L NaClO with different concentration of LiOH at 180 ^oC (d).

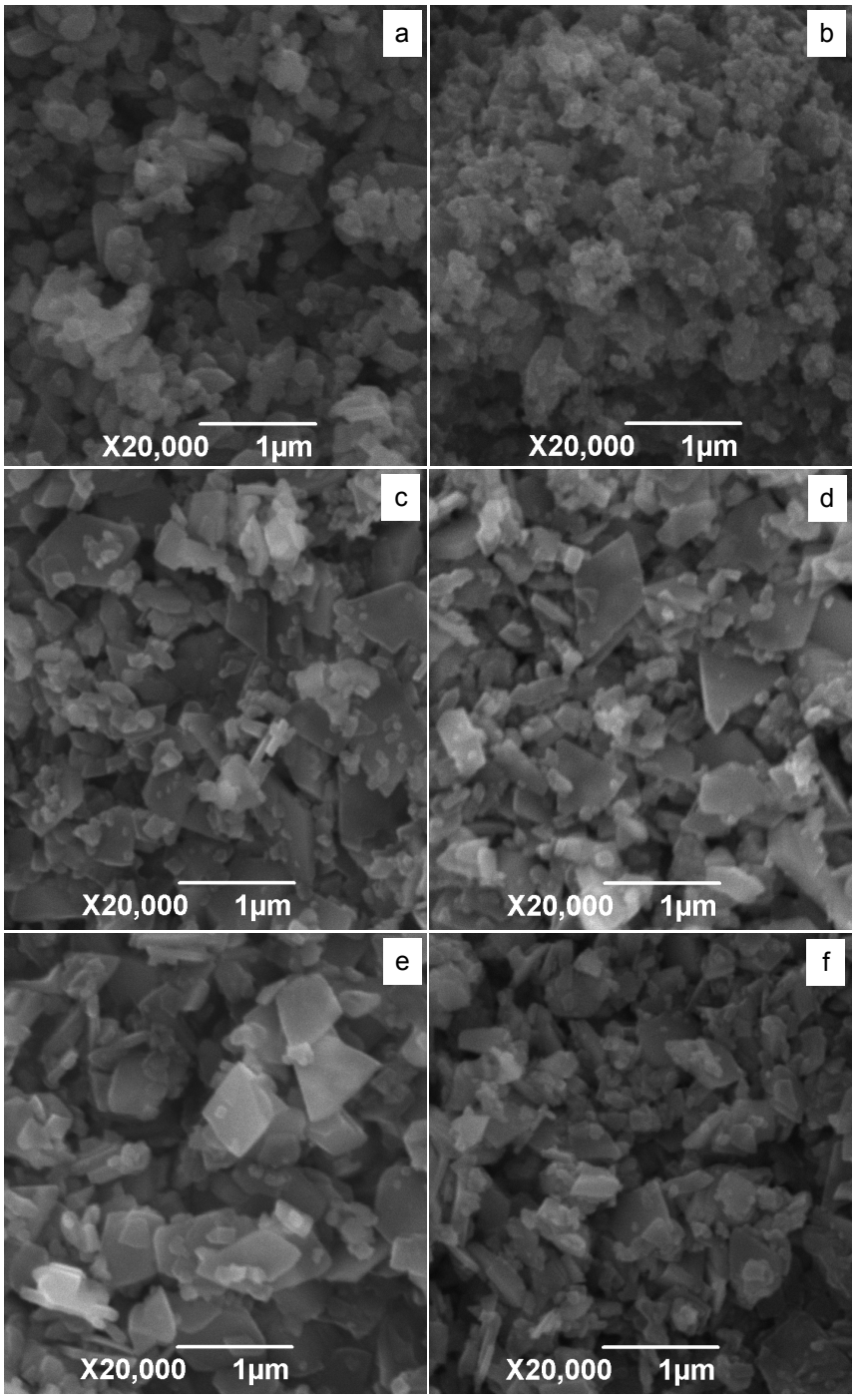

Fig. 2. SEM images of M_0 (a), M_m (b), M_3 (c), M_6 (d), M_9 (e) and M_{12} (f).

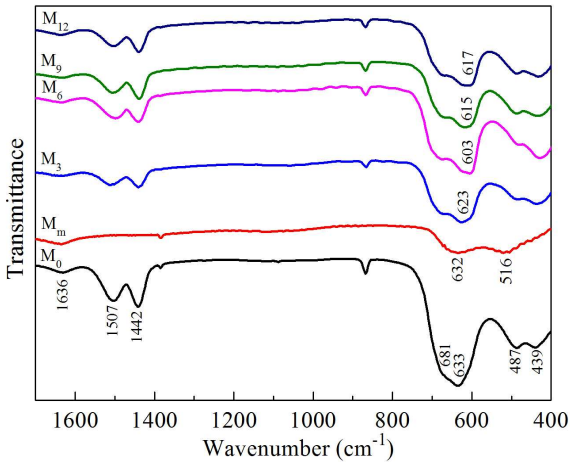

Fig. 3. FTIR spectra of M_0, M_m, M_3, M_6, M_9, and M_{12}.

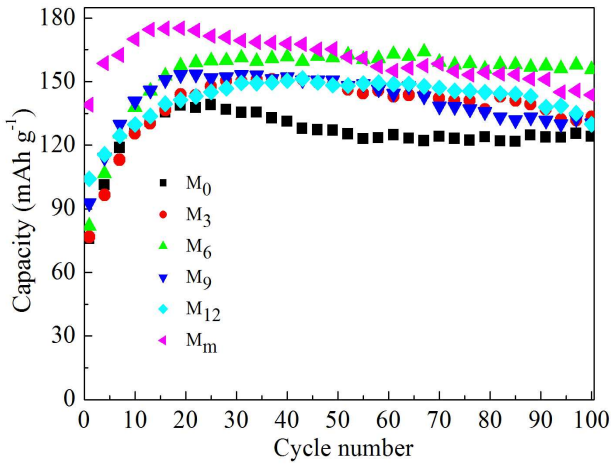

Fig. 4. Discharge specific capacity *vs*. cycle number at the current density of 100 mA g^{-1} for M_0, M_3, M_6, M_9, M_{12}, and M_m after heat-treatment at 110 ^oC for 12 h.

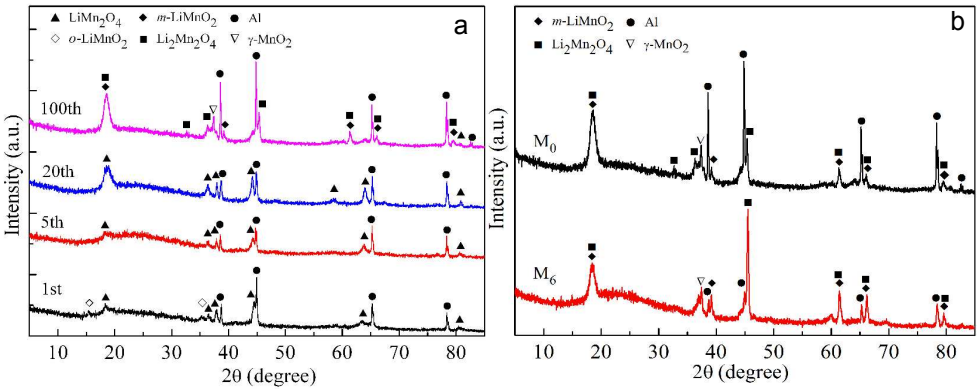

Fig. 5. XRD patterns of intermediate products after different cycles of charge/discharge test for M_0 (a), and 100 cycles of charge/discharge test for M_0 and M_6 (b).

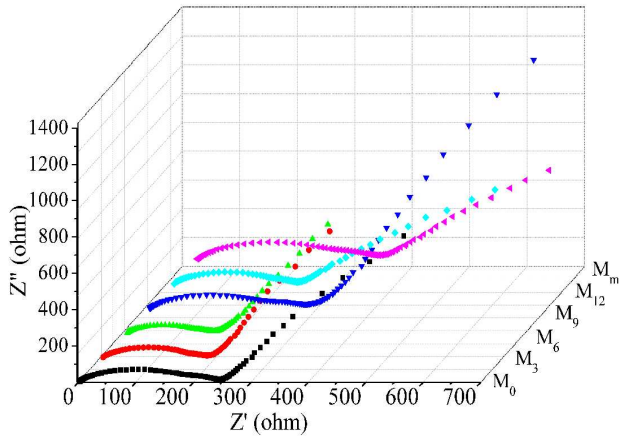

Fig. 6. Electrochemical impedance spectra of M_0, M_3, M_6, M_9, M_{12}, and M_m as Nyquist plots measured at 25 ^oC before charge/discharge test.

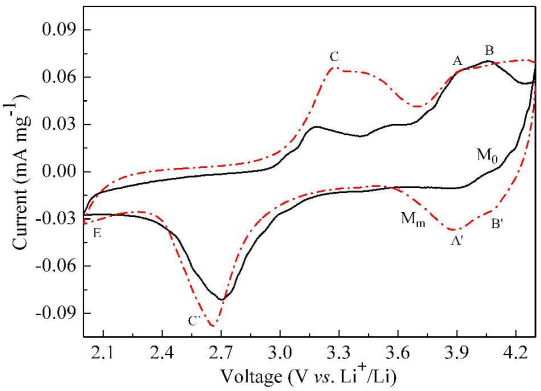

Fig. 7. Cyclic voltammograms of M_0 and M_m in 1.0 mol L^{-1} $LiClO_4$ +EC+DMC+EMC with equal volume within potential range of 2.0-4.3 V (*vs*. Li/Li^+) with a scan rate of 0.1 mV s^{-1}.

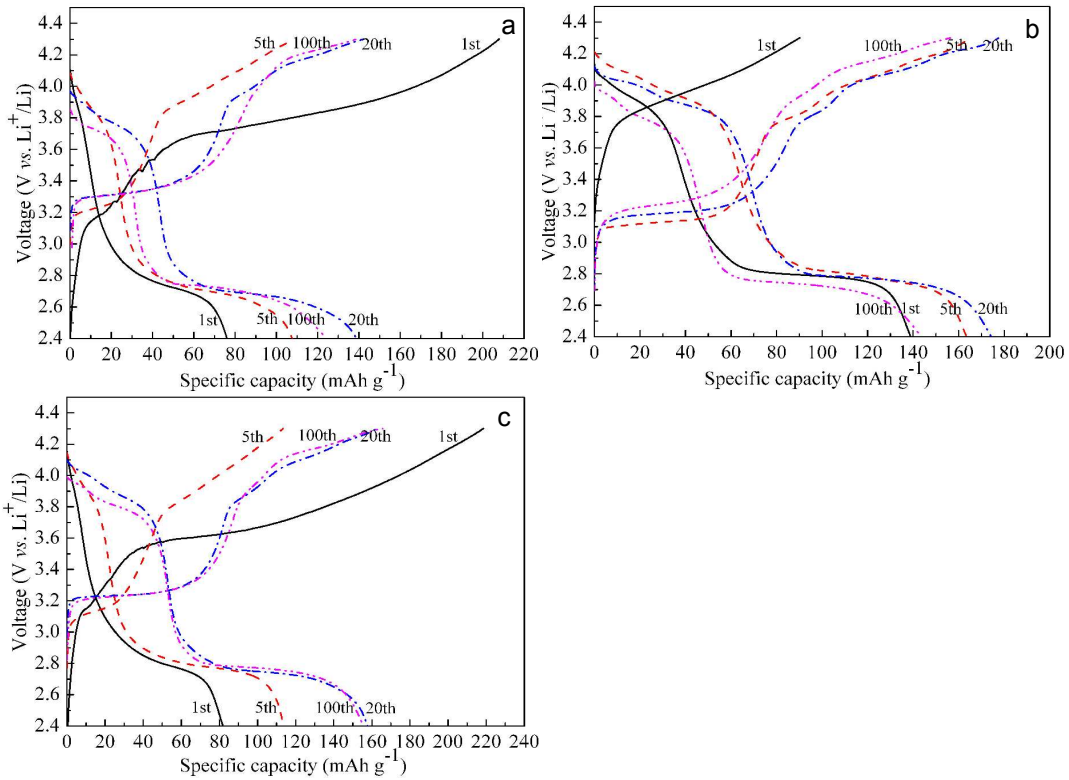

Fig. 8. Discharge/recharge profiles of M_0 (a), M_m (b), and M_6 (c) for different cycles at a current density of 100 mA g^{-1}.